Focusing and stabilizing laser–plasma-generated electron beams with magnetic devices

2014 Jpn. J. Appl. Phys. 53 092702

(http://iopscience.iop.org/1347-4065/53/9/092702)

Japanese Journal of Applied Physics **53**, 092702 (2014) **REGULAR PAPER**
http://dx.doi.org/10.7567/JJAP.53.092702

Focusing and stabilizing laser–plasma-generated electron beams with magnetic devices

Yuji Oishi[1,2,3*], Danilo Giulietti[2,4,3], Federica Baffigi[3], Lorenzo Fulgentini[3], Antonio Giulietti[3], Petra Köster[3], Luca Labate[3,2], Masaki Kando[5], and Leonida A. Gizzi[3,2]

[1]*Central Research Institute of Electric Power Industry, Yokosuka, Kanagawa 240-0196, Japan*
[2]*Istituto Nazionale di Fisica Nucleare, Sez. Pisa, 56127 Pisa, Italy*
[3]*Intense Laser Irradiation Laboratory, Istituto Nazionale di Ottica, Consiglio Nazionale delle Ricerche, 56124 Pisa, Italy*
[4]*Dipartimento di Fisica, Universita di Pisa, 56127 Pisa, Italy*
[5]*Japan Atomic Energy Agency, Kizugawa, Kyoto 619-0215, Japan*
E-mail: oishi@criepi.denken.or.jp

Received February 24, 2014; accepted July 6, 2014; published online August 19, 2014

External magnetic devices have been successfully tested to control the divergence and pointing stability of subrelativistic electron beams accelerated by ultrashort laser pulses in a nitrogen plasma (electron density of $\sim 10^{19}\,\mathrm{cm}^{-3}$). Different configurations of the magnetic devices have been studied, and their effects are discussed in detail. The analysis is also supported by the results of ray-tracing simulations using the first-order trajectory equation in the magnetic field configurations. This simple method of improving beam stability will be particularly useful for applying laser-generated ultrashort electron beams to high-dose radiobiological studies. © 2014 The Japan Society of Applied Physics

1. Introduction

Laser–plasma acceleration driven by an ultrashort (10–100 fs) intense laser pulse has the potential to provide a new class of compact electron accelerators because the electric fields can reach 100 GV/m, which is 10^3 times higher than those in conventional accelerators.[1)] In fact, the generation of quasi-monoenergetic GeV-level electrons has recently been experimentally demonstrated in an acceleration path with a length of cm order.[2,3)] The consequent drastic reduction in the dimensions and cost of the apparatus opens, in principle, the door to various applications, including a compact source of X–γ radiation and secondary particles.[4–8)] In addition to the compactness of accelerators, using an ultrashort beam structure, ultrafast pulse radiolysis[9)] and biomedical applications[10,11)] have also been proposed. Moreover, these sources are intrinsically synchronized with laser systems, satisfying the optimal conditions for femtosecond time-resolved pump–probe measurements in the basic and applied sciences.

For the above applications, the control of the electron beams is a key issue. Among the techniques for controlling the stability of electron beams generated by laser–plasma acceleration, the use of an external static magnetic field[12,13)] is one of the most promising, along with the use of colliding optical injection,[14,15)] a plasma density gradient,[16)] gases with a high atomic number,[17–19)] and prepulse suppression.[20,21)] Our method, in which an external static magnetic field is also applied along the laser propagation axis, produces electron beams with high beam-pointing stability and low emittance. However, as we will show, our devices mainly act on electrons escaping from the plasma accelerator. Our experiments should therefore be distinguished from previous experiments aimed at improving acceleration performances by magnetically modifying the laser–plasma interaction. The latter was attempted in the study of Hosokai et al., who reported stable collimated electron beams with Maxwellian energy distributions using a 12 TW, 40 fs laser pulse with a static magnetic field of 0.2 T,[12)] and ~100 MeV quasi-monoenergetic electron beams were produced using a 7 TW, 45 fs laser pulse with a strong magnetic field of 1 T.[13)]

In both experiments reported in Refs. 12 and 13, the laser intensity I was of $\sim 10^{19}\,\mathrm{W/cm^2}$ order and a helium (He) gas jet was used as the target. On the other hand, Mori et al. pointed out the possibility that the formation of the acceleration field depends on the gas material.[17)] The present work has been aimed at improving the performance of a laser-driven electron source mostly devoted to biomedical studies such as electron radiography[22)] and radiobiology. Such a source provides high-charge electron beams of subrelativistic energy and a broad spectrum consistent with a Maxwellian distribution of temperature $k_B T \sim 200$ keV. Such an energy level reduces the electron range in water to a fraction of a millimeter. This feature, combined with the ultrashort duration of the beam ($\tau \sim 3.5$ ps) and the high charge, results in an outstanding instantanous dose rate ($\sim 10^9$ Gy/s) never delivered before to a biological thin sample. This rate can be further increased by focusing the electrons on the sample. Furthermore, systematic radiobiological investigations require good control of electron beam pointing. Both issues can be addressed by adding suitable magnetic devices to the laser-driven accelerator. We prove here that an axial magnetic field generated by a suitable and simple device enables the stabilization and control of the dose distribution on samples.

The next section is devoted to a description of the experiments, including the main setup and the magnetic devices in its various configurations. In Sect. 3, the effects of the magnetic devices on both the angular distribution of electrons and the pointing stability of the beam are presented, analyzed, and discussed, including through ray-tracing simulation. Conclusions are drawn in Sect. 4.

2. Methods and devices

Figure 1(a) shows a schematic drawing of the overall experimental setup. The experiments were carried out using a Ti:sapphire laser (Amplitude Technologies) based on a chirp pulse amplification (CPA) technique that can deliver up to 120 mJ, 40 fs pulses at a fundamental wavelength of 800 nm with a repetition rate of 10 Hz. In this study, the energy delivered to the target was 100 mJ and laser irradiation was conducted in the single-shot mode. An $f/5$ off-axis, Au-coated parabolic mirror was used to focus the laser light. 50% of the p-polarized laser light was contained in a focal spot of 10 μm in full width at half maximum (FWHM). The nominal laser intensity at the focal spot was estimated to be

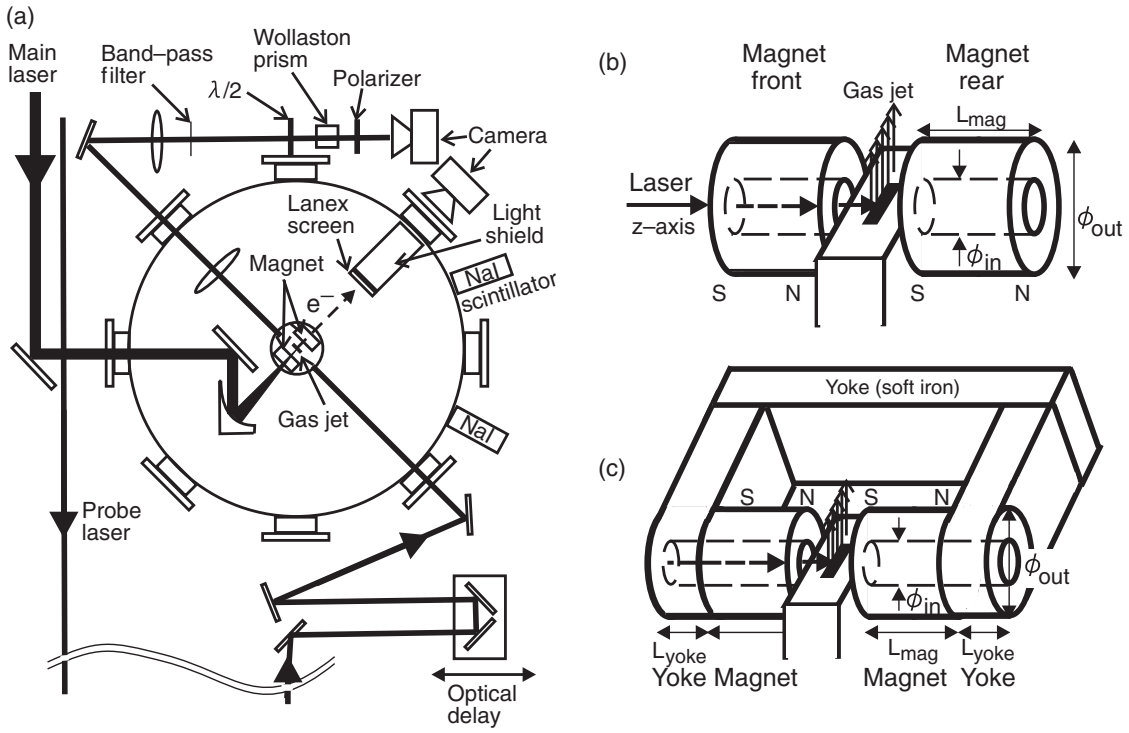

Fig. 1. (a) Schematic drawing of the experimental setup. Magnification of the area around the slit nozzle (b) without a yoke and (c) with a yoke.

$I \sim 3 \times 10^{18}\,\mathrm{W/cm^2}$. The corresponding normalized vector potential a_0 is 1.2. The contrast between the main pulse and the 3 ns prepulse owing to the amplified spontaneous emission (ASE) was 2.5×10^7.

As an acceleration medium, the gas from a supersonic N_2 gas jet device consisting of a solenoid fast pulse valve (SmartShell A2-6443-FL, LX-03R) and a rectangular slit nozzle of 1.2 mm length and 4.0 mm width was used.[23,24] We set the short side of the nozzle parallel to the laser axis direction. In these experiments, the stagnation pressure of the valve was 38 bar and, at this pressure, the maximum plasma density n_e was measured to exceed $10^{19}\,\mathrm{cm^{-3}}$ with ionization degree $Z = 5$. Both the neutral gas and plasma densities were measured by interferometry, while the degree of ionization was inferred by numerical simulation.[25] At a gas atomic density exceeding $2 \times 10^{18}\,\mathrm{cm^{-3}}$, the ns prepulse intensity exceeding $10^{11}\,\mathrm{W/cm^2}$ was sufficient to preform a plasma in the focal region before the arrival of the main pulse. The gas and its density, contrast and focal position in the gas jet were chosen and tuned in order to obtain the optimal conditions and high-charge, broad-spectrum beams of sub-relativistic electrons. For the measurement of the electron energy and charge, a stack of dosimetric films (Gafchromic MDV255) and plastic layers was used similarly to a "SHEEBA" device.[26] The dosimetric films were situated at depths of 1, 3, 5, and 10 mm inside the stack, thus allowing the detection of electrons with energies greater than 400 keV. An aluminum (Al) filter of 15 μm thickness was placed in front of the stack to avoid direct laser irradiation. The electron beam has a Maxwellian spectrum with a temperature of ~300 keV and a charge on the order of 100 pC. However, the electron beam was rather divergent and the pointing stability of the electron beam was very poor, as discussed in detail in Sect. 3. Thus, we decided to test the effectiveness of external magnetic fields for a) controlling the beam divergence and possibly shaping the electron distribution on the sample and b) improving the shot-to-shot pointing stability.

Table I. Configurations of the magnetic devices.

Configuration	Magnet size ($\mathrm{mm^3}$) $\phi_{out} \times \phi_{in} \times L_{mag}$	Installation side	Yoke ($\mathrm{mm^2}$) $\phi_{in} \times L_{yoke}$
Case 0	—	No magnet	—
Case I	14 × 8 × 15	Front and rear	—
Case II	15 × 6 × 12	Front and rear	—
Case III	15 × 6 × 12	Only rear	—
Case IV	15 × 6 × 12	Front and rear	6 × 6

Our magnetic device consists of ring-shaped neodymium permanent magnets, coupled as shown in either Fig. 1(b) or 1(c). The gas jet slab lay in the midplane of the "sandwich" and the laser–plasma interaction region was on the main axis of the device. The magnet conditions in different experiments are indicated in Table I. In case I (II), the inner hole diameter of the magnet is 8 (6) mm and the thickness is 15 (12) mm. One magnet was set in front of the nozzle and the other was set symmetrically on the rear side of the nozzle. Across the interaction region the magnetic field was parallel to the laser axis, which is indicated as the z-axis. In case III, only one magnet was used (with the same size as in case II) on the rear side. In case IV, a c-shaped yoke consisting of soft-iron plates was attached to the pair of magnets [Fig. 1(c)]. The iron plate in direct contact with the ring magnet has a hole of the same diameter as that of the ring magnet, allowing the propagation of the laser or electron beam. The distance between the front and rear magnets, including the holders, was 15 mm, while the distance between the laser focal point and the rear magnet was 7.5 mm. The distribution of the magnetic field along the laser axis direction [$B(z)$] in each case was measured externally, as

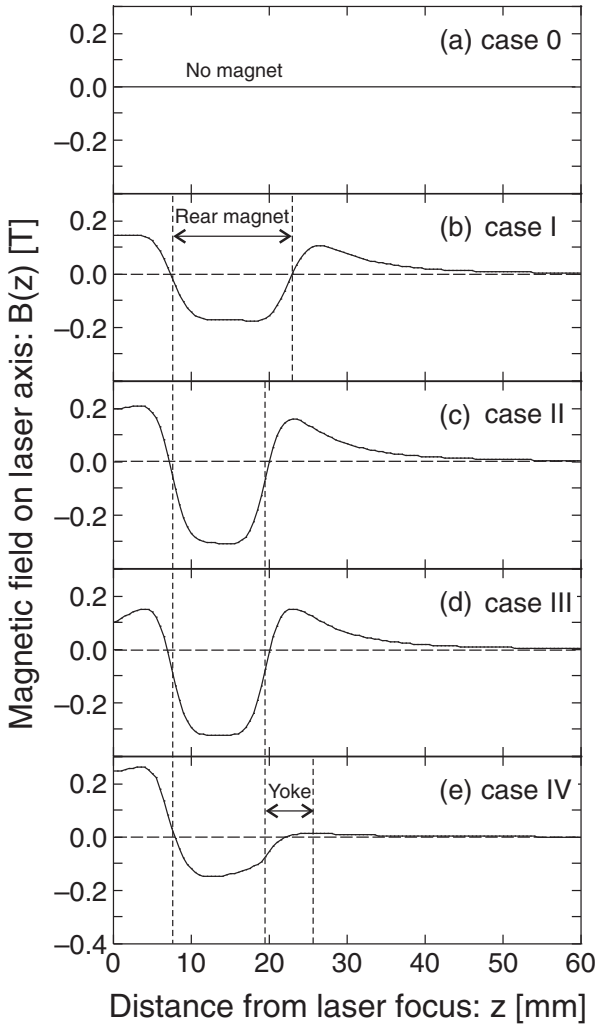

Fig. 2. Magnetic fields along the laser axis [$B(z)$]. (a)–(e) correspond to cases 0–IV in Table I, respectively.

shown in Fig. 2, where $z = 0$ is the laser focal point. $B(z)$ in the inner hole was calculated using numerical codes.[27,28)]

$B(z)$ is smaller in case I than in case II because the inner hole diameter is larger than that in case II. In case III, the magnet is set only on the rear side of the gas jet and $B(z)$ is symmetrical with respect to the center of the rear magnet. Here, although the magnetic field around the gas jet [$B(z \simeq 0)$] is smaller than that in case II, $B(z)$ in the vicinity of the rear magnet is similar to that in case II. In case IV, owing to the presence of the c-shaped iron yoke, a magnetic circuit is formed and $B(z \simeq 0)$ is enhanced, while $B(z)$ in the inner hole and outside the yoke is reduced.

Electrons accelerated by laser plasma were detected on a phosphor screen (Lanex Kodak Fine screen)[29)] with a diameter of 50 mm, which was located 85 mm from the target. The Lanex screen was covered with 12-μm-thick Al foil used as a light shield. Its image was observed with a digital camera (Pentax K200) set up outside the vacuum chamber.

To know the plasma density distribution, we set up an interferometer as shown in Fig. 1(a). A fraction of the main femtosecond pulse was frequency-doubled by employing a 2-mm-thick, type-I LBO crystal and used as an optical probe propagating perpendicular to the main pulse in a Normarski interferometer configuration.[30)] The probe pulse duration was estimated to be ∼200 fs in FWHM. Interferograms were taken at different delays between the probe and the main pulse. The most interesting interferograms for our purpose were taken immediately before the arrival of the main pulse at the nominal focus, as discussed in detail in Sect. 3. Here we only note that a preplasma produced by ASE is clearly visible before the arrival of the main pulse. Moreover, there is clear evidence of perturbations of the main pulse propagation due to both hosing instability in the laser–plasma interaction and refraction from the preplasma boundaries. Similar preplasma effects on ultrashort pulse propagation have been previously observed.[31)]

3. Results and discussion

Typical electron distribution images on the Lanex screen are shown in Fig. 3 (left side). Figures 3(a)–3(e) correspond to cases 0–IV in Table I, respectively. The color scale on the top of Fig. 3(a) is common for Figs. 3(a)–3(e). The transverse profile of the electron beam in the horizontal axis is also inset for cases I–IV. Each image was obtained with a single shot. In case 0 (no magnetic field), the spatial distribution of the electron is broad over the screen and the intensity of the electron beam is weak. Nevertheless, a faint structure can be observed in the cross section of the electron beam. (See also the inset, in which the brightness scale is different from that in the color figures to show the faint structure.) This structure is roughly a quasi-ring shape with a large aperture, in which the central region has lower intensity.

On the other hand, with a magnetic field, the results can be classified into two groups. One group includes cases I and IV, in which the electron beam is observed within a portion of a circle with a diameter of ∼20 mm and the peak intensity of the beam is approximately twice that in case 0. The pattern does not always have the same geometry as that in Fig. 3(b), but usually the central part is less intense than the peripheral part [Fig. 3(e)].

The other group includes cases II and III, in which the spatial distribution is very narrow and the peak intensity of the beam is approximately 5 times higher than that in case 0. The electron beam spot size in FWHM, as an average of ∼20 shots, is 4.6 mm in case II and 8.8 mm in case III, which correspond to divergence angles of 55 ± 29 and 103 ± 60 mrad, respectively.

The beam pointing (peak point) in each shot is plotted in Fig. 3 (right side). Each figure contains 20–30 shots. In case 0, the beam pointing fluctuates shot by shot and the root-mean-square (rms) beam pointing from the centroid of all the beam pointing is ±184 mrad, which is denoted by a circle drawn with a broken line in Fig. 3(f). In the central part, within ±87 mrad, which corresponds to the emission angle of 5° from the focus, there is an almost empty area. The inner circle drawn with a dashed line in Fig. 3(f) shows this border, inside of which there are few beam pointing. In contrast, pointing is very stable in cases II and III, with most shots located within ±2.4 mrad for case II and ±15 mrad for case III. In cases I and IV, it is interesting to note that the peak points lie approximately on a circle in both cases, similarly to the electron distribution in each shot.

The results described above are clear evidence of a strong effect of the magnetic field on the electron trajectories, as expected. Before analyzing this effect in detail, let us

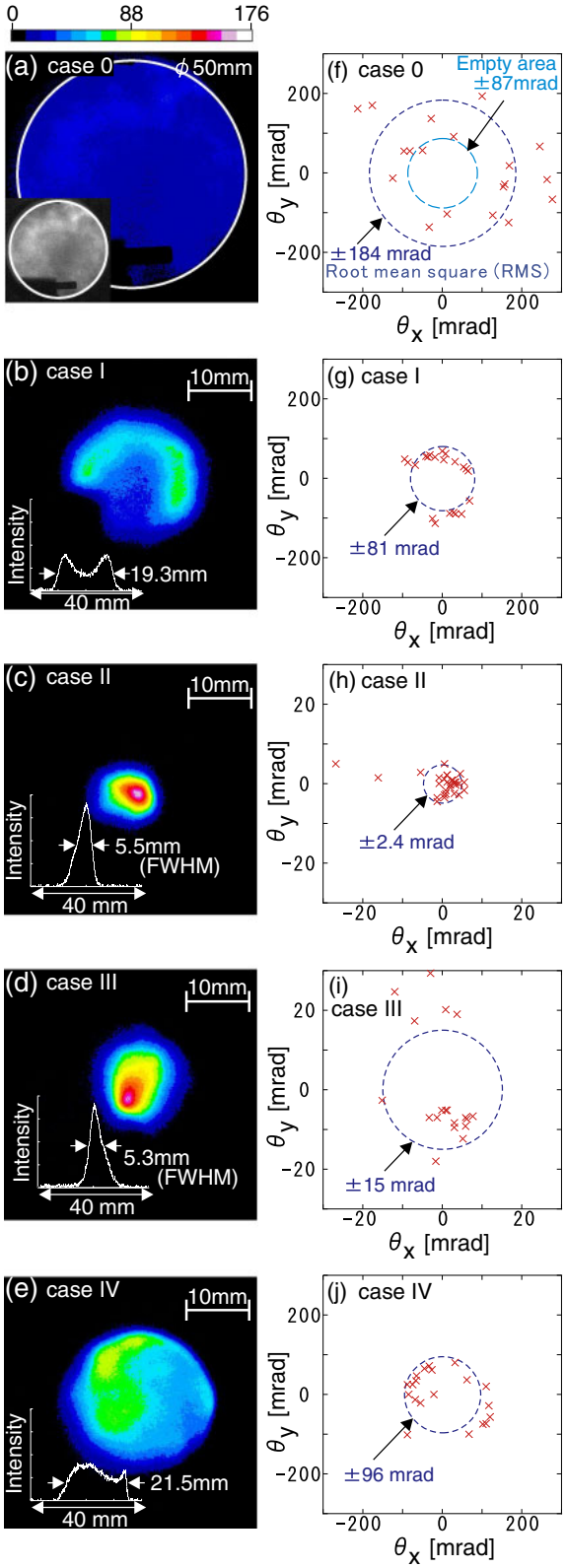

Fig. 3. (Color online) Left (a)–(e): Typical electron images on the Lanex screen. Each image was obtained with a single shot. Right (f)–(j): Beam-pointing stability. Each figure contains 20–30 shots. Figures on the left and right correspond to each other. (a)–(e) correspond to cases 0–IV in Table I, respectively.

introduce two other possible contributions. The first is due to electron beam cutting by the inner hole(s) of the magnet(s). The second one could be due to the magnetic field effect on the laser–plasma interaction, which was reported in Ref. 12.

First let us consider the electron beam angular limits imposed by the magnet holes. This has an obvious effect that will be accounted for in the following, but it is not sufficient to explain our observations if the magnetic effect is not considered. For example, the electron beams in case II are more focused than those in case IV, whereas the geometrical collimation length, which is defined as the sum of the thicknesses of the rear magnet and the yoke, in case II is shorter than that in case IV. In addition, as another example, the degrees of collimation of the electron beams in cases I and IV are similar, whereas the geometrical collimation length is longer and the magnet aperture is smaller in case IV than those in case I. Thus, the external magnetic field must affect the focusing of electron beams. We should take note of the results for case III in particular. In this successful case, the ring magnet was set only on the rear side of the gas jet [right-hand side in Fig. 1(b)], and $B(z=0) \simeq 0.1\,\mathrm{T}$, which is smaller than that in case II ($\sim$0.2 T). In contrast, in case IV, although $B(z=0)$ is larger than that in case II, the electron beam is not very focused. Therefore, $B(z)$ in the region behind the laser–plasma interaction is more important than $B(z=0)$ for focusing. In the successful cases II and III, the maximum $|B(z)|$ in the rear magnet is larger than 0.2 T. Thus, from the experimental viewpoint, the value of 0.2 T seems a typical value for categorizing the results of our experiments into two groups.

Concerning the effects of the magnetic field on the laser–plasma interaction and electron acceleration, the mechanism of focusing electron beams is explained in Ref. 12 by considering that preplasma produced by a laser prepulse in the vicinity of the laser focal point is modified by the external magnet field under the condition $\omega_L \tau_{ei} > 1$, where ω_L is the Larmor frequency and τ_{ei} is the electron–ion collision time. Consequently, the preplasma changes from an elliptical cavity into a two-cone structure with a density peak at the laser focal point. This plasma shape suppresses the diffraction of the main laser pulse, and efficient and stable self-injection can occur. However, in our experiments, the two-cone structure was never observed, regardless of whether or not the magnetic field was applied. This is consistent with the overall data analysis, leading to the conclusion that under our conditions the external magnetic field mainly acts on the electron beams escaping from the plasma. Since our laser intensity is one order of magnitude lower and the contrast ratio is better than those in Ref. 12, the temperature of the preformed plasma is expected to be only $T_e \sim 200\,\mathrm{eV}$ for the prepulse with $I = 6 \times 10^{11}\,\mathrm{W/cm^2}$, $\sim$1% of the main pulse energy, and a duration of 2 ns. The magnetized condition appears to be difficult to satisfy in our case because the threshold of the magnetic field is estimated to be $\sim$0.5 T by considering $\tau_{ei} \propto T_e^{1.5}/(Z^2 N_i \Lambda)$, where Z is the ion charge, N_i is the ion density, and Λ is the Coulomb logarithm.

Figure 4(a) shows a typical interferogram of the plasma 0.9 ps before the main pulse arrived at the laser focus in case II. At this time, the main pulse has not yet reached the preformed plasma. The interferogram in Fig. 4(b) was taken 0.4 ps later. At this later time, the main pulse interacts with the preplasma. It is interesting to observe that the high-density shock wave surrounding the preplasma deflects part of the incoming pulse. The deflection angle (θ_{df}) of the laser pulse in Fig. 4(b) is estimated to be approximately 5°. This

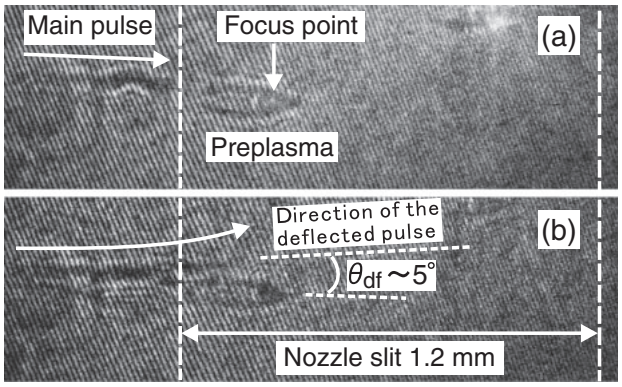

Fig. 4. Typical interferogram of the plasma in case II (a) 0.9 ps and (b) 0.5 ps before the main pulse arrives at the laser focus. Vertical dashed lines indicate the limits of the nozzle slit. At the position of the laser entrance (530 μm above the nozzle plane), the gas jet expanded outside these limits. This explains why the ionized region produced by the main, very intense, pulse is also visible outside the entrance boundary of the nozzle.

value is coincident with the angle of the border (±87 mrad) in Fig. 3(f), inside of which there are few beam pointing. This may result in the quasi-ring-shaped intensity distribution around the axis. This effect has been observed[31] and can partially explain the ring-shaped feature we observed on the Lanex screen, as we will discuss below.

To estimate the magnetic-lens effect, we performed ray-tracing simulations using the first-order trajectory equation in the magnetic fields:

$$r'' + \frac{eB(z)^2}{8m_e\hat{\Phi}}r = 0, \quad (1)$$

where r is the transverse coordinate, e is the electron fundamental charge, m_e is the electron mass, and $\hat{\Phi}$ is the relativistic acceleration potential.[32] Figures 5(a)–5(e) show the simulated electron traces in magnetic fields in cases 0–IV, respectively, for an electron point source of 200 keV, which is the threshold value of the Lanex screen.[29] The dashed box in Figs. 5(b)–5(e) shows the boundary of the inner hole diameter of the ring magnet. Traces for different emission angles at the point source were simulated, but only the traces of electrons that do not touch the boundary and can reach the screen are shown in the figures. The diameter on the screen determined by this limitation is denoted as ϕ_{bm}. Among the traces, the results for emission angles at the point source of less than θ_{df} are shown as dotted curves. The diameter on the screen determined by the boundary between traces for emission angles of less than θ_{df} and those for more than θ_{df} is denoted as ϕ_{df}. These results are in very good agreement with the experimental results [Figs. 3(b)–3(e)]. One can clearly see that the grouping of cases into (I, IV) and (II, III) occurs. The differences in the beam sizes on the screen between the experimental and simulated results are probably caused by the assumption of a point source and a monoenergetic electron beam. Furthermore, disregarding the aberrations in the simulation results in a sharpened beam size. It should be realized that both the electron energy and the sample-screen position are critical when comparing our ray-tracing results with our experimental results. What we can conclude is that ray tracing definitely confirms that magnetic configurations I and IV *cannot* focus our beams on the sample, regardless

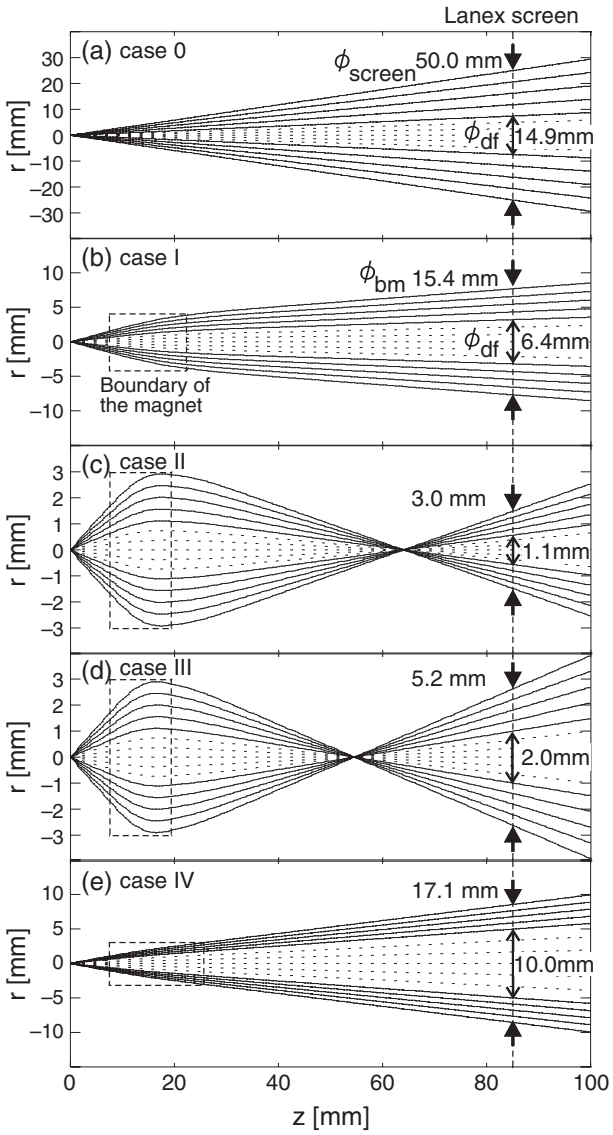

Fig. 5. Calculated 200 keV electron traces in the magnetic fields. The dashed box shows the boundary of the internal diameter of the ring magnet, which determines ϕ_{bm}. On the other hand, ϕ_{df} is determined by the boundary between traces for emission angles of less than θ_{df}, which are shown as dotted curves in the figures, and those for more than θ_{df}, which are shown as solid curves. (a)–(e) correspond to the results of cases 0–IV in Table I, respectively.

of where the sample is located, while the beam *can* be focused with stable pointing on a sample with configurations II and III.

Concerning the quasi-ring shapes observed in Fig. 3, we consider that (i) the main laser pulse is deflected by the boundary of the preformed plasma (see also Ref. 31), (ii) the main direction of electron acceleration becomes slightly different from the magnetic field axis (z-axis), which causes the lower intensity of the center part on the screen image, and (iii) most of the electron beam reaches the screen between ϕ_{bm} and ϕ_{df}. Although $\phi_{df} = 6.4$ mm in case I, which corresponds to ±38 mrad, is smaller than the experimental value [Fig. 3(g)], $\phi_{df} = 10.0$ mm in case IV, which corresponds to ±117 mrad, is close to the experimental value [Fig. 3(j)]. In cases II and III, it is difficult to discriminate between ϕ_{df} and ϕ_{bm} in the experimental results, probably because the electrons are not monoenergetic.

4. Conclusions

Using four different magnetic configurations, we improved the pointing and focusing of subrelativistic electron beams accelerated by laser interaction at $I \sim 10^{18}\,\mathrm{W/cm^2}$ with a N_2 gas jet, producing a plasma of $n_e \sim 10^{19}\,\mathrm{cm^{-3}}$. The experimental results show that under our conditions the external static magnetic field mainly acts on the electron beam escaping from the laser-target interaction region. The modified electron distribution on the sample screen is a combined effect of magnetic optics and beam tailoring produced by the magnet entrance hole. The electron beam cross section on the sample was reduced from more than 50 mm to about 5 mm, and the pointing instability was almost suppressed from about 200 mrad to a few mrad. Our observations were in good agreement with those calculated from the magnetic-lens effect via ray tracing for electrons of 200 keV kinetic energy. In fact, the massive electron population with energy around this value was consistent with the spectral evaluation. For practical uses, the whole magnetic device can be reduced to magnet(s) set at the output of the electron beam. In principle, this method can allow the control of focusing/defocusing and positioning of a laser-generated electron beam on a sample simply by using ring magnets of a suitable size and field strength, which can be calculated via numerical ray tracing. Furthermore, by setting a suitable iris on the focal plane of a given energetic component, a quasi-monoenergetic electron beam can be selected. Once refined, our magnetic device can be easily added to any existing laser accelerator to improve its performances in view of future applications of laser-driven electron beams, such as in radiobiology, radiotherapy, radiology, and radiography.

Acknowledgments

The authors acknowledge fruitful discussions with G. Bussolino, G. Cristoforetti, and T. Levato of Consiglio Nazionale delle Ricerche. We also thank S. Eto, T. Fujii, T. Amakawa, and K. Nemoto of Central Research Institute of Electric Power Industry for their support and helpful discussions.

1) T. Tajima and J. M. Dawson, Phys. Rev. Lett. **43**, 267 (1979).
2) W. P. Leemans, B. Nagler, A. J. Gonsalves, Cs. Toth, K. Nakamura, C. G. R. Geddes, E. Esarey, C. B. Schroeder, and S. M. Hooker, Nat. Phys. **2**, 696 (2006).
3) N. M. Hafz, T. M. Jeong, I. W. Choi, S. K. Lee, K. H. Pae, V. V. Kulagin, J. H. Sung, T. J. Yu, K.-H. Hong, T. Hosokai, J. R. Cary, D.-K. Ko, and J. Lee, Nat. Photonics **2**, 571 (2008).
4) Y. Glinec, J. Faure, L. Le Dain, S. Darbon, T. Hosokai, J. J. Santos, E. Lefebvre, J. P. Rousseau, F. Burgy, B. Mercier, and V. Malka, Phys. Rev. Lett. **94**, 025003 (2005).
5) M. Kando, Y. Fukuda, A. S. Pirozhkov, J. Ma, I. Daito, L.-M. Chen, T. Zh. Esirkepov, K. Ogura, T. Homma, Y. Hayashi, H. Kotaki, A. Sagisaka, M. Mori, J. K. Koga, H. Daido, S. V. Bulanov, T. Kimura, Y. Kato, and T. Tajima, Phys. Rev. Lett. **99**, 135001 (2007).
6) A. Giulietti, N. Bourgeois, T. Ceccotti, X. Davoine, S. Dobosz, P. D'Oliveira, M. Galimberti, J. Galy, A. Gamucci, D. Giulietti, L. A. Gizzi, D. J. Hamilton, E. Lefebvre, L. Labate, J. R. Marques, P. Monot, H. Popescu, F. Reau, G. Sarri, P. Tomassini, and P. Martin, Phys. Rev. Lett. **101**, 105002 (2008).
7) C. Gahn, G. D. Tsakiris, G. Pretzler, K. J. Witte, C. Delfin, C.-G. Wahlstrom, and D. Habs, Appl. Phys. Lett. **77**, 2662 (2000).
8) L. A. Gizzi, M. P. Anania, G. Gatti, D. Giulietti, G. Grittani, M. Kando, M. Krus, L. Labate, T. Levato, Y. Oishi, and F. Rossi, Nucl. Instrum. Methods Phys. Res., Sect. B **309**, 202 (2013).
9) D. A. Oulianov, R. A. Crowell, D. J. Gosztola, I. A. Shkrob, O. J. Korovyanko, and R. C. Rey-de-Castro, J. Appl. Phys. **101**, 053102 (2007).
10) V. Malka, J. Faurea, and Y. A. Gauduel, Mutat. Res. Rev. Mutat. Res. **704**, 142 (2010).
11) L. Labate, M. G. Andreassi, F. Baffgi, G. Basta, R. Bizzarri, A. Borghini, G. C. Candiano, C. Casarino, M. Cresci, F. Martino, L. Fulgentini, F. Ghetti, M. C. Gilardi, A. Giulietti, P. Koster, F. Lenci, T. Levato, Y. Oishi, G. Russoe, A. Sgarbossa, C. Traino, and L. A. Gizzi, Proc. SPIE **8779**, 87790O (2013).
12) T. Hosokai, K. Kinoshita, A. Zhidkov, A. Maekawa, A. Yamazaki, and M. Uesaka, Phys. Rev. Lett. **97**, 075004 (2006).
13) T. Hosokai, A. Zhidkov, A. Yamazaki, Y. Mizuta, M. Uesaka, and R. Kodama, Appl. Phys. Lett. **96**, 121501 (2010).
14) J. Faure, C. Rechatin, A. Norlin, A. Lifschitz, Y. Glinec, and V. Malka, Nature **444**, 737 (2006).
15) H. Kotaki, I. Daito, M. Kando, Y. Hayashi, K. Kawase, T. Kameshima, Y. Fukuda, T. Homma, J. Ma, L.-M. Chen, T. Zh. Esirkepov, A. S. Pirozhkov, J. K. Koga, A. Faenov, T. Pikuz, H. Kiriyama, H. Okada, T. Shimomura, Y. Nakai, M. Tanoue, H. Sasao, D. Wakai, H. Matsuura, S. Kondo, S. Kanazawa, A. Sugiyama, H. Daido, and S. V. Bulanov, Phys. Rev. Lett. **103**, 194803 (2009).
16) C. G. R. Geddes, K. Nakamura, G. R. Plateau, Cs. Toth, E. Cormier-Michel, E. Esarey, C. B. Schroeder, J. R. Cary, and W. P. Leemans, Phys. Rev. Lett. **100**, 215004 (2008).
17) M. Mori, K. Kondo, Y. Mizuta, M. Kando, H. Kotaki, M. Nishiuchi, M. Kado, A. S. Pirozhkov, K. Ogura, H. Sugiyama, S. V. Bulanov, K. A. Tanaka, H. Nishimura, and H. Daido, Phys. Rev. ST Accel. Beams **12**, 082801 (2009).
18) M. Mori, Laser Kenkyu **40**, 826 (2012) [in Japanese].
19) A. Pak, K. A. Marsh, S. F. Martins, W. Lu, W. B. Mori, and C. Joshi, Phys. Rev. Lett. **104**, 025003 (2010).
20) S. P. D. Mangles, A. G. R. Thomas, M. C. Kaluza, O. Lundh, F. Lindau, Z. Najmudin, C. G. Wahlstrom, C. D. Murphy, C. Kamperidis, K. L. Lancaster, E. Divall, and K. Krushelnick, Plasma Phys. Control. Fusion **48**, B83 (2006).
21) E. Miura and S. Masuda, Appl. Phys. Express **2**, 126003 (2009).
22) G. C. Bussolino, A. Faenov, A. Giulietti, D. Giulietti, P. Köester, L. Labate, T. Levato, T. Pikuz, and L. A. Gizzi, J. Phys. D **46**, 245501 (2013).
23) T. Hosokai, K. Kinoshita, T. Watanabe, K. Yoshii, T. Ueda, A. Zhidkov, and M. Uesaka, Proc. 8th European Particle Accelerator Conf., 2002, p. 981.
24) T. Hosokai, K. Kinoshita, K. Nakamura, T. Watanabe, K. Yoshii, T. Ueda, A. Zhidkov, M. Uesaka, H. Kotaki, M. Kando, and K. Nakajima, Phys. Rev. E **73**, 036407 (2006).
25) A. Giulietti, A. Andre, S. Dobosz Dufrenoy, D. Giulietti, T. Hosokai, P. Koester, H. Kotaki, L. Labate, T. Levato, R. Nuter, N. C. Pathak, P. Monot, and L. A. Gizzi, Phys. Plasmas **20**, 082307 (2013).
26) M. Galimberti, A. Giulietti, D. Giulietti, and L. A. Gizzi, Rev. Sci. Instrum. **76**, 053303 (2005).
27) Web [http://www.neomag.jp/mag_navi/tool_top.php] [in Japanese].
28) Web [http://laacg.lanl.gov/laacg/services/download_sf.phtml].
29) Y. Glinec, J. Faure, A. Guemnie-Tafo, V. Malka, H. Monard, J. P. Larbre, V. De Waele, J. L. Marignier, and M. Mostafavi, Rev. Sci. Instrum. **77**, 103301 (2006).
30) R. Benattar, C. Popovics, and R. Sigel, Rev. Sci. Instrum. **50**, 1583 (1979).
31) A. Giulietti, P. Tomassini, M. Galimberti, D. Giulietti, L. A. Gizzi, P. Köester, L. Labate, T. Ceccotti, P. D'Oliveira, T. Auguste, P. Monot, and P. Martin, Phys. Plasmas **13**, 093103 (2006).
32) W. Glaser, Z. Phys. **117**, 285 (1941) [in German].